Nanoporous Silicon Structures for Toxin Detection

H. Ghosh[*1], C. RoyChaudhuri[1]
[1]Bengal Engineering and Science University Shibpur (BESUS), Howrah-711103, West Bengal
*hrilina12@gmail.com

Abstract: In this paper, a high-performance nanocrystalline porous silicon-based impedance sensor has been reported for the sensitive detection of Aflatoxin B1 (AFB1). Nanoporous silicon with pore thickness of about 100 nm has been simulated using COMSOL Multiphysics software for studying the distribution of electric field lines on the sensor surface. The same was fabricated on a silicon wafer by anodical etching. The samples were then oxidized to obtain different oxide thickness of 0.15 μm and 0.05 μm. Next electrodes were fabricated followed by optimized silanization and antibody immobilization. Toxin detection was based on the change in the double layer impedance at the oxide-electrolyte interface caused by specific antigen-antibody binding. The developed sensor was observed to be highly sensitive, detecting AFB1 of concentration as low as 100 fg/ml with a significant sensitivity of around 40%. Hence, it has the potential to detect toxin molecule down to 10 fg/ml.

Keywords: nanocrystalline porous silicon, toxin detection, impedance biosensor, high-performance, interdigitated.

1. Introduction

Aflatoxins are naturally occurring mycotoxins produced by fungi. Among naturally occurring Aflatoxins, Aflatoxin B1 (AFB1) is the most abundant and is carcinogenic. Aflatoxin contamination has been reported in several food items like cereals, grains, peanuts etc. Human beings are exposed to aflatoxins either directly by eating toxin contaminated food products or indirectly via animal products. Once formed, Aflatoxins are hard to destroy as they are relatively heat stable [1].

Hence extensive research is required in aflatoxin detection because of the danger it poses to human health. High-performance liquid chromatography (HPLC) and thin-layer chromatography (TLC) are some of the methods for the detection of toxins. Although accurate and sensitive, the main disadvantage of chromatographic methods is that they need expensive equipments.

Electrochemical sensors are a good choice due to their simple, fast and low-cost detection capabilities for biological binding events [2]. An impedimetric biosensor based on DNA and gold nanoparticles was developed for the detection of Aflatoxin M1 (AFM1) [3]. However, DNA processing and immobilization is both a complex and costly procedure. A signal-amplified electrochemical immunosensor for detection of AFB1 in rice was developed [1]. However, this sensor was not label-free. The sensitivity was also not high with a detection limit of only 0.1 ng/ml. Mycotoxin detection by STING (Signal Transduction by Ion Nano-Gating) [4] is a label-free sensor capable of achieving excellent detection limits of 100 fg/ml. However, the success rate in achieving the target pore size for the nanopipette which forms the STING sensor is only 25% and hence is difficult for reproducible fabrication. Thus nanopipette fabrication is the highest source of inefficiency for the development of STING sensor. A majority of the existing methods for biomolecule detection relies on the capture of the antigen by the antibody immobilized on the sensor surface [5-8]. However, for small molecular size and low weight toxins like aflatoxin, the main problem is that the toxin molecules are so small in size that they are almost entirely enveloped by the primary capture antibody, thus being unable to cause significant change.

A recent report on nanoporous impedimetric biosensor [9] for detection of trace atrazine from water samples shows a detection limit of 10 fg/ml. Here, nanoporous alumina in the biosensor device generates a high density array of nanoscale confined spaces. This demonstrates that biomolecule activity is maximized when the molecules are confined in regions having dimensions comparable to those of the biomolecules. However, there is no report on the use of nanoporous substrates for high sensitive toxin detection.

In this paper, we have simulated and fabricated nanocrystalline porous silicon substrates for sensitive detection of AFB1. The

nanoporous silicon substrate with simple lateral electrode configuration has the capability of effectively confining electric field lines which may result in improved sensitivity compared to nanoporous alumina substrates.

2. Use of COMSOL Multiphysics

Nanoporous silicon substrate having pores with thickness of about 100 nm is expected to act as a better trapping medium for toxin molecules and also possesses higher sensitivity as impedance sensor, even in presence of widely spaced electrodes, than the planar substrate. This has been verified by observing the electric field line pattern obtained by simulating a few nanoporous silicon 3D structures using COMSOL Multiphysics (version 3.5a) ['Conductive Media DC' under MEMS module].

2.1 Structure 1

The cross-sectional view and top view of Structure 1 are shown in Fig. 1(a) and 1(b) respectively. The nanopores are of dimensions 50 nm × 50 nm × 100 nm. The silicon regions are oxidized and the pores are filled with a conducting medium since the starting platform for antibody immobilization is an oxidized nanoporous silicon substrate. The ratio (R) of the height of the pores to the distance between the electrodes is roughly 1:5.

Subdomain conditions applied are as follows:
Silicon substrate – conductivity 10 S/m.
Oxide – conductivity 10^{-18} S/m.
Electrodes – conductivity
Solution in pores – conductivity 10 S/m.

Boundary conditions applied are as follows:
All faces of electrode 1 – 10 V.
All faces of electrode 2 – ground.
All external faces – electric insulation.
All internal faces – continuity.

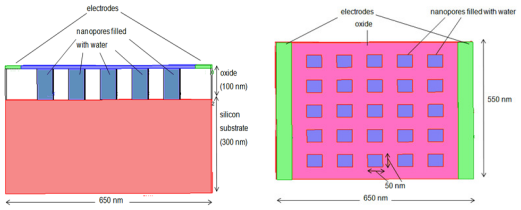

(a) (b)

Figure 1. (a) Cross-sectional view and (b) top view of Structure 1

After simulation, the current flow distribution obtained is shown in Fig. 2. It is observed that majority of the current lines from the electrodes enter the pores and then pass through the silicon substrate as it provides a relatively low impedance parallel path compared to the lateral current path. Thus, the field lines are laterally confined to only a small portion near the electrode irrespective of the horizontal and vertical spread of the applied solution.It has been observed that almost 75% of the current lines are confined within a distance of 150 nm from the electrode edge which shows that even for large electrode spacing there will be sufficient confinement of the current lines within the nanometric biomolecules.

2.2 Structure 2

The cross-sectional view and top view of Structure 2 are shown in Fig. 3(a) and 3(b) respectively. The nanopores are of dimensions 100 nm × 100 nm ×100 nm. R is roughly 1:10. Subdomain and boundary conditions are same as before.

After simulation, the current flow distribution obtained is shown in Fig. 4. This

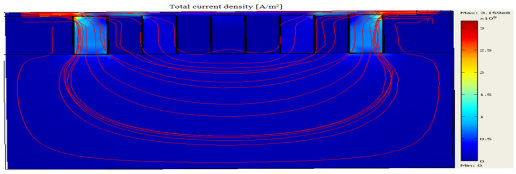

Figure 2. Current flow distribution of Structure 1

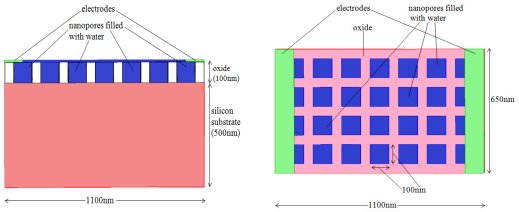

(a) (b)

Figure 3. (a) Cross-sectional view and top view of Structure 2

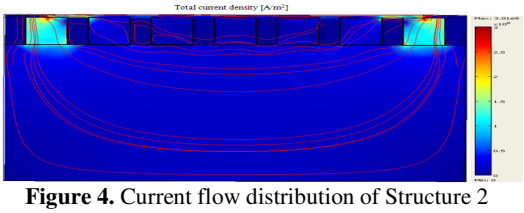

Figure 4. Current flow distribution of Structure 2

time, it is observed that almost 85% of the current lines are confined within a distance of 150 nm from the electrode edge. So, we see that as R decreases, horizontal current flow through the top solution layer further decreases and there is better confinement of the electric field lines.

In the fabricated samples, R is much less than 1:10. In other words, the distance between the electrodes is actually much larger than the thickness of the nanopores and hence confinement of the current lines is expected to be even more effective.

2.3 Structure 3

The cross-sectional view and top view of Structure 3 are shown in Fig. 5(a) and 5(b) respectively. The nanopores are of dimensions 200 nm × 200 nm × 200 nm. R is roughly 1:10. Different pore dimensions are considered to study the effect of different oxide thickness on nanoporous silicon. Subdomain and boundary conditions are same as before.

After simulation, the current flow distribution obtained is shown in Fig. 6. We observe that with larger diameter of the pores, confinement of current lines near the pores is poor which may be attributed to the fact that the oxide thickness is less and hence the effective resistance of the remaining region decreases.

The variation in current as we move along the sample surface away from the electrode in both Structure 2 and Structure 3 is shown in Fig. 7. The maximum current at the electrode edges is denoted as *Is* for both structures. We observe that the current decreases on the top lateral surface as we move away from the electrodes in both structures.

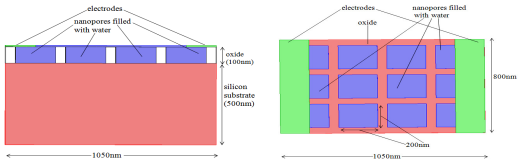

(a) (b)

Figure 5. (a) Cross-sectional view and (b) top view of Structure 3

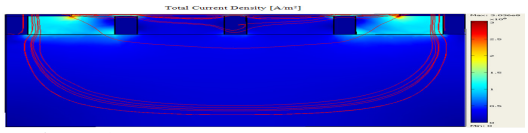

Figure 6. Current flow distribution of Structure 3

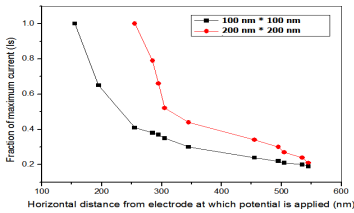

Figure 7. Variation of current along sample surface for both Structure 2 and Structure 3

2.4 Structure 4 and Structure 5

Structure 4 and Structure 5 are actually modified from Structure 2 as can be seen in Fig. 8(a) and 8(b) respectively. Structure 4 has spherical cells of diameter 20 nm having conductivity 1 S/m on the top solution surface, excluding regions above the pores. Structure 5 is different from Structure 4 only in that it contains cells within the nanopores as well. Subdomain and boundary conditions are same as before.

After simulation, current flow distributions of Structure 4 and Structure 5 are shown in Fig. 9(a) and 9(b) respectively. We observe that compared to Structure 2, current density decreases in both Structure 4 and Structure 5 due to the presence of the spherical molecules. Further, in Structure 5 as the number of cells is more than that in Structure 4, current density further decreases in Structure 5. This can also be clearly seen in Fig. 10(a) and 10(b) which compares the current density of Structure 2 with that of Structure 4 and Structure 5 respectively.

2.5 Structure 6 and Structure 7

Structure 6 and Structure 7 are actually modified from Structure 3 as can be seen in Fig. 11(a) and 11(b) respectively. Structure 6 has

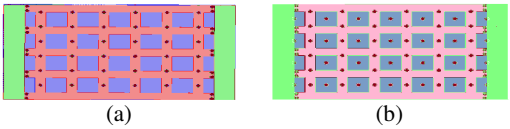

(a) (b)

Figure 8. Top views of (a) Structure 4 and (b) Structure 5

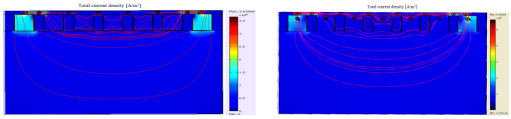

(a) (b)

Figure 9. Current flow distributions of (a) Structure 4 and (b) Structure 5

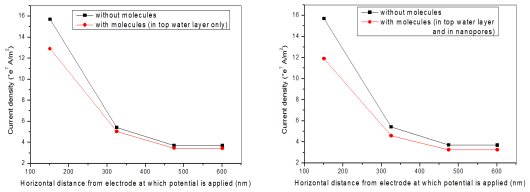

(a) (b)

Figure 10. Current density comparison along sample surface of Structure 2 with (a) Structure 4 and (b) Structure 5

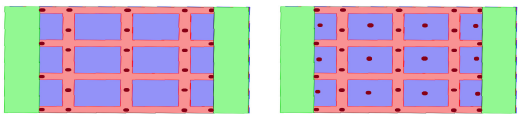

(a) (b)

Figure 11. Top views of (a) Structure 6 and (b) Structure 7

spherical cells of diameter 20 nm having conductivity 1 S/m on the top solution surface, excluding regions above the pores. Structure 7 is different from Structure 6 only in that it contains cells within the nanopores as well. Subdomain and boundary conditions are same as before.

After simulation, the current flow distributions of Structure 6 and Structure 7 are shown in Fig. 12(a) and 12(b) respectively. We observe that compared to Structure 3, current density decreases in both Structure 6 and Structure 7 due to the presence of the spherical molecules. Further, in Structure 7 as the number of cells is more than that in Structure 6, current density further decreases in Structure 7. This can also be clearly seen in Fig. 13(a) and 13(b)

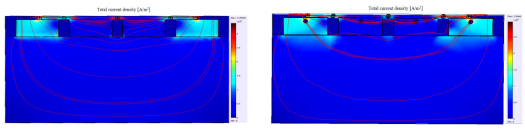

(a) (b)

Figure 12. Current flow distributions of (a) Structure 6 and (b) Structure 7

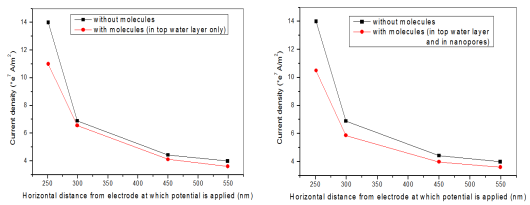

(a) (b)

Figure 13. Current density comparison along sample surface of Structure 3 with (a) Structure 6 and (b) Structure 7

which compares the current density of Structure 3 with that of Structure 6 and Structure 7 respectively.

3. Materials and Methods

3.1 Fabrication of Nanocrystalline Porous Silicon

For fabrication of nanoporous silicon, p-type <100> silicon wafers of resistivity 10-20 Ωcm were cleaned by standard procedure and then etched anodically in a double pond electrochemical bath with an electrolytic mixture of hydrofluoric acid (48 wt%) and dimethyl sulfoxide in the ratio 1:9 by volume [10]. Etching an area of 1.6 cm^2 was carried out under a constant current source of 2.35 mA for 30 minutes to obtain pores of thickness of about 100 nm and diameter of about 250 nm. SEM images of the nanocrystalline porous silicon thus formed are shown in Fig. 14(a) and 14(b).

3.2 Thermal Oxidation and Metallization

Dry thermal oxidation has been done in an oxidation furnace at 1000 ºC for 3 hours and 90 minutes to obtain oxide thickness of 0.15 µm and 0.05 µm respectively.

For metallization, metal electrodes of high temperature silver paste have been fabricated using screen printing technique and then cured at 750ºC for 1 minute. After that, gold metal is evaporated on silver. Fig. 15 shows the final view of the sensor.

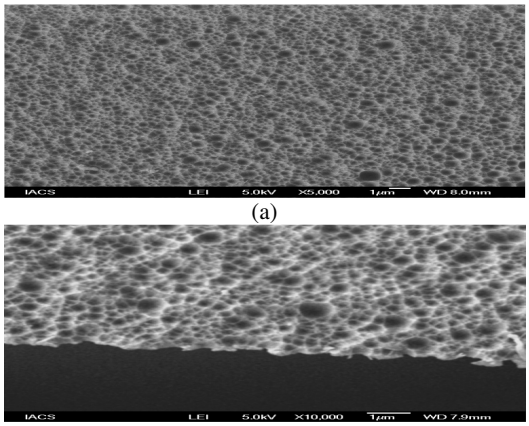

(a)

(b)

Figure 14. SEM images of the (a) cross-section and (b) top surface of the nanoporous silicon formed

Figure 15. Final view of the sensor

3.3 Surface Functionalization and Antibody Immobilization

For surface functionalization [11], the oxidized samples were treated with sulphochromic acid for 10 minutes followed by treatment with hydroxylated silane (MTS) on dancing shaker for 1 hour. Next, samples were incubated at 95 ºC and then treated with cross-linker 2 mM GMBS. Finally anti-AFB1 antibody (ATB1) was immobilized.

3.4 Toxin Sample Preparation

AFB1 of concentration 10 ng/ 50 µl was procured from a microbiological laboratory at the Indian Institute of Chemical Biology. For calibrated measurements, serial dilutions of this toxin solution were made with PBS to yield AFB1 toxin solution of concentration 0.1 pg/ml.

3.5 Impedance Measurement

The sensors were characterized electrically with an LCR meter between 100 Hz and 100 kHz with an applied voltage of 50 mV. Steady state impedance and phase readings were recorded with sensors exposed to 30 µl of Phosphate Buffered Saline (PBS) before and after antibody immobilization and after exposure to toxin solution for 30 minutes.

3.6 SEM and EDX Measurement

SEM and EDX analysis were done by JSM 6700F JEOL, Japan instrument. SEM characterization was done at an operating voltage of 5 kV, 10 µA, working distance of 8 mm. EDX analysis was done at an operating voltage of 20 kV, 20 µA, working distance of 15 mm.

4. Results and Discussions

4.1 EDX Analysis

This is done to determine presence of nitrogen. Before antibody immobilization, nitrogen is absent in the samples. After antibody immobilization, samples were found to contain nitrogen which has probably been contributed by the antibody molecules. Hence, EDX analysis confirms the immobilization of antibody on the sensor surface. Table 1 shows the results of the EDX analysis.

4.2 Impedance Measurement

Impedance measurement is done by the LCR meter in Z/Ø mode by considering the sensor as an equivalent capacitance (*Cp*) in parallel with a shunt resistance (*Rp*).

4.2.1 Measurement in absence of antibody

Fig. 16(a) and 16(b) show the variation in impedance and variation in phase with frequency respectively for two different thickness of the oxide layer before antibody immobilization. Impedance decreases with frequency for both

Table 1: Results of EDX Analysis

Element	Weight%	Atomic%
Carbon	12.92	16.36
Nitrogen	6.50	7.05
Oxygen	80.59	76.59
Total	**100.00**	**100.00**

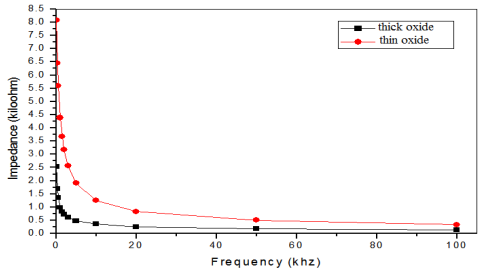

(a)

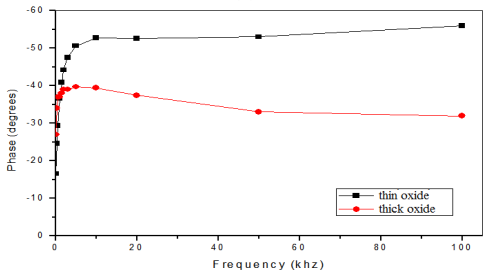

(b)

Figure 16. Variation in (a) impedance and (b) phase with frequency before antibody immobilization

samples because the double layer impedances at the electrode-electrolyte interface and the oxide-electrolyte interface decrease with frequency as power law.

From Fig. 16(a), it is seen that the sample with thinner oxide offers greater impedance than the sample with thicker oxide. This can be explained with the help of Fig. 17 which depicts an electrical model of nanoporous silicon in presence of liquid. *Zsole* and *Zsolo* are the double layer impedances at the electrode-solution interface and oxide-solution interface respectively. *Rsol* and *R1sol* are effective solution resistances above the sensor surface and in the pores respectively. *Rbulk* is the resistance of the bulk silicon substrate. With increase in oxide thickness, the effective transmission line impedance *Zt* decreases and so, thinner oxide offers more impedance than thicker oxide.

4.2.2 Measurement in presence of antibody

Fig. 18 shows the variation in impedance with frequency for two different thickness of oxide layer after antibody immobilization. Comparing with Fig. 16(a), we see that impedance decreases for thin oxide and increases for thick oxide. After antibody immobilization, *Zt* decreases and *Zsole* increases for both samples. But for thin oxide, the effect of *Zt* dominates over the effect of *Zsole* and so, impedance decreases. But for thick oxide, the effect of *Zsole* is more than that of *Zt* and hence, impedance increases.

Fig. 19 shows the percentage change in impedance with frequency before and after antibody immobilization. For both samples, percentage change and hence sensitivity increases with frequency. At lower frequency, the sample with thick oxide shows greater sensitivity than that with thin oxide because at lower frequency, effect of *Zsole* dominates and in thick oxide, effect of *Zsole* is more than that in thin oxide.

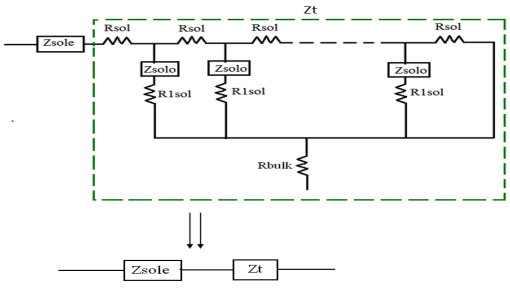

Figure 17. Electrical model of nanoporous silicon in presence of liquid

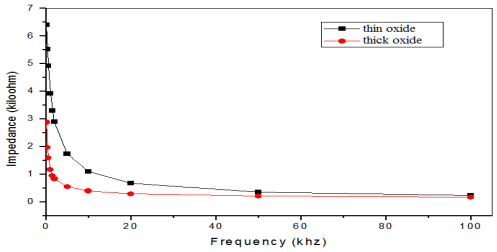

Figure 18. Variation in impedance with frequency after antibody immobilization

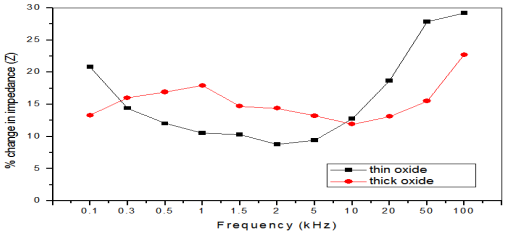

Figure 19. Percentage change in impedance with frequency after antibody immobilization

4.2.3 Measurement after addition of AFB1

Fig. 20 shows the variation in impedance with frequency before and after capture of toxin molecules. Impedance changes significantly due to change in the double layer impedance caused by specific antigen-antibody binding event that took place on the sensor surface. Fig. 21 shows the percentage change in impedance with frequency after capture of toxin molecules. Sensitivity increases with frequency and is maximum (about 40% to 44%) in the range of 5 kHz to 20 kHz.

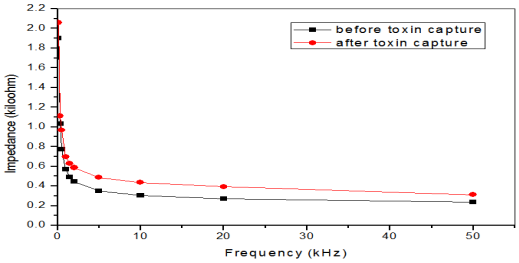

Figure 20. Variation in impedance with frequency before and after capture of toxin molecules

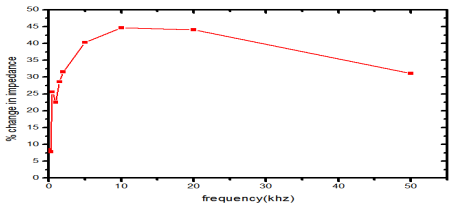

Figure 21. Percentage change in impedance with frequency after toxin detection

5. Conclusion

In this paper, a high-performance nanocrystalline porous silicon impedance biosensor has been realized with an optimum pore depth of 100 nm for the sensitive detection of AFB1. First, a few nanoporous silicon structures were simulated using COMSOL software for studying the distribution of electric field lines on the sensor surface. Next, the sensors were fabricated and measurements recorded. The developed sensor is highly sensitive and could detect AFB1 at a concentration of 100 fg/ml. Since the developed sensor is simple and has been observed to be highly sensitive, detecting AFB1 of concentration as low as 100 fg/ml with a significant sensitivity of around 40%, it has the potential to detect toxin molecule down to 10 fg/ml which is lower than all existing reports of electrical sensors for toxin detection.

6. References

1. Yun Tan, Xia Chu, Guo-Li Shen, Ru-Qin Yu, A signal-amplified electrochemical immunosensor for Aflatoxin B1 determination in rice, *Analytical Biochemistry,* **387,** 82-86 (2009)
2. E. Bakker, Y. Qin, Electrochemical Sensors, *Analytical Chemistry,* **78**, 3965-3983 (2006)
3. Erhan Dinckaya, Özer Kınık, Mustafa Kemal Sezgintürk, Ca˘grı Altu˘g, Aylin Akkoca, Development of an impedimetric Aflatoxin M1 biosensor based on a DNA probe and gold nanoparticles, *Biosensors and Bioelectronics,* **26**, 3806-3811 (2011)
4. Paolo Actisa, Olufisayo Jejelowob, Nader Pourmand, Ultrasensitive mycotoxin detetction by STING sensors, *Biosensors and Bioelectronics,* **26**, 333-337 (2010)
5. S. Piermarini, L. Micheli, N.H.S. Ammida, G. Palleschi, D. Moscone, Electrochemical immunosensor array using a 96-well screenprinted microplate for Aflatoxin B1 detection, *Biosensors and Bioelectronics,* **22**, 1434-1440 (2007)
6. Madhu Prakash Chatrathi, Joseph Wang, Greg E. Collins, Sandwich electrochemical immunoassay for the detection of Staphylococcal Enterotoxin B based on immobilized thiolated antibodies, *Biosensors and Bioelectronics,* **22**, 2932-2938 (2007)
7. Charlie O. Parker, Ibtisam E. Tothill, Development of an electrochemical immunosensor for Aflatoxin M1 in milk with focus on matrix interference, *Biosensors and Bioelectronics*, **24**, 2452-2457 (2009)
8. Lucian-Gabriel Zamfir, Irina Geana, Sondes Bourigua, Lucian Rotariu, Camelia Bala, Abdelhamid Errachid, Nicole Jaffrezic-Renault, Highly sensitive label-free immunosensor for ochratoxin A based on functionalized magnetic nanoparticles and EIS/SPR detetction, *Sensors and Actuators B*, **159**, 178-184 (2011)
9. Pie Pichetsurnthorna, Krishna Vattipalli, Shalini Prasad, Nanoporous impedimetric biosensor for detetction of trace atrazine from water samples, *Biosensors and Bioelectronics*, **32**, 155-162 (2012)
10. Ramkrishna Dev Das, Abhishek Dey, Sumantra Das, Chirasree RoyChaudhuri, Interdigitated electrode-less high-performance macroporous silicon structure as impedance biosensor for bacteria detection, *IEEE Sensors Journal*, **Vol. 11, No. 5,** (2011)
11. R. Dev Das, S. Maji, S. Das, C. RoyChaudhuri, Optimization of covalent antibody immobilization on macroporous silicon solid supports, *Applied Surface Science,* **256**, 5867-5875 (2010)

7. Acknowledgements

The authors would like to acknowledge NPMASS, ADA for providing financial support for the software. The authors are grateful to Dr. S. Das and Dr. T. Dhar of the Indian Institute of Chemical Biology, Jadavpur for providing the toxin samples. The authors would also like to thank Mr. Debasis Mondal of the Department of Electronics and Telecommunication, Bengal Engineering and Science University Shibpur and Mr. Ramkrishna Dev Das of the Saha Institute of Nuclear Physics for their valuable help and guidance.